Chinese Chemical Letters 36 (2025) 109675

Contents lists available at ScienceDirect

Chinese Chemical Letters

journal homepage: www.elsevier.com/locate/cclet

Pseudocapacitance dominated Li_3VO_4 encapsulated in N-doped graphene *via* 2D nanospace confined synthesis for superior lithium ion capacitors

Caili Yang[a,b], Tao Long[b], Ruotong Li[b], Chunyang Wu[a,*], Yuan-Li Ding[b]

[a] National Key Laboratory of Electronic Thin Film and Integrated Devices, University of Electronic Science and Technology of China, Chengdu 611731, China
[b] College of Materials Science and Engineering, Hunan University, Changsha 410082, China

ARTICLE INFO

Article history:
Received 12 December 2023
Revised 14 January 2024
Accepted 22 February 2024
Available online 23 February 2024

Keywords:
Lithium ion capacitor
Li_3VO_4
Graphene
Anode
Pseudocapacitance

ABSTRACT

A pseudocapacitance dominated anode material assembled from Li_3VO_4 nanocrystals encapsulated in the interlayers of N-doped graphene has been developed *via* a facile 2D nanospace confined strategy for lithium ion capacitors (LICs). In this contribution, the N-doped graphene synthesized by a faicle solid state reaction using C_3N_4 nanosheets as template and glucose as carbon source provides sufficient 2D nanospace for the confined and homogeneous growth of Li_3VO_4 at the nanoscale, and simultaneously efficiently anchors each nanobuilding block inside the interlayers, thus realizing the utilizaiton of full potential of active components. The so-formed 3D hybrids not only ensure intimate electronic coupling between active materials and N-doped graphene, but also realize robust structure integrity. Owing to these unique advantages, the resulting hybrids show pseudocapacitance dominated lithium storage behaviors with capacitive contributions of over 90% at both low and high current rates. The LVO@C@NG delivers reversible capacities of 206 mAh/g at 10 A/g, capacity retention of 92.7% after 1000 cycles at 2 A/g, and a high energy density of 113.6 Wh/kg at 231.8 W/kg for LICs.

Lithium ion capacitor (LIC), as a kind of hybrid electrochemical energy storage device, has attracted extensive attention since it can well balance high-energy density of batteries and high-power density of capacitors within one device [1–4]. Typically, for this device, one eletrode stores charge through battery-typed faradaic redox reaction, and the other one is based on surface-controlled physical behavior with ion adsorption and desorption like electric double layer capacitor (EDLC) [5–7]. However, typical battery materials stored large amounts of energy (~200 Wh/kg) often take several hours in charging owing to slowly diffusion-limited redox reactions while capacitive materials store much smaller amounts of energy (~5 Wh/kg) by rapidly forming the electrical double layers on the order of seconds. Such a large imbalance difference in the reaction kinetics between cathode and anode seriously restricts practical application of LICs. In this regard, developing a suitable anode material with rapid redox kinetics for well matching capacitive cathode of LICs is imperative but still remains a great challenge.

To address the above issue, pseudocapacitive materials offer an opportunity to simultaneously realize high energy density and high power density because it can exhibit battery-like redox reactions that occur at a current density comparable to those of electronic double layer formation of capacitive materials [8]. For example, Nb_2O_5 exhibits a notable surface-charge storage contribution (>80%) with ion diffusion kinetics [9], which is not limited by semi-infinite diffusion. Similar to Nb_2O_5, TiO_2 (B) also shows fast Li^+ ion intercalation behaviors with surface-controlled redox reaction since the cyclic voltammetry analysis is nearly linear dependent on the peak current on the sweep rate [10,11]. On the other hand, electrochemical behaviors of some battery materials strongly depend on the particle size. With reduction of particle dimensions, they exhibit a pseudocapacitive response as well. For instance, the well-known $LiCoO_2$ cathode in LIBs delivers a typical capacitive profile when the particle size is reduced to 10 nm [12]. Such capacitive behaviors are attributed to the decrease in the electronic and ionic diffusion pathways, suppression of phase transitions, and an enhancement of available surface sites for Li^+ transport [13]. As for MoO_2, when the particle size is reduced to 20 nm, it exhibits a specific capacity of 120 mAh/g at 10 C [14], three times higher than that of micro-sized counterpart (40 mAh/g). Furthermore, by introducing graphene, the as-prepared MoO_2/graphene hybrid shows a higher capacity of 150 mAh/g at an ultrahigh current rate (50 C). Therefore, the combination of reducing particle size and introduc-

* Corresponding author.
E-mail address: wucy@uestc.edu.cn (C. Wu).

https://doi.org/10.1016/j.cclet.2024.109675
1001-8417/

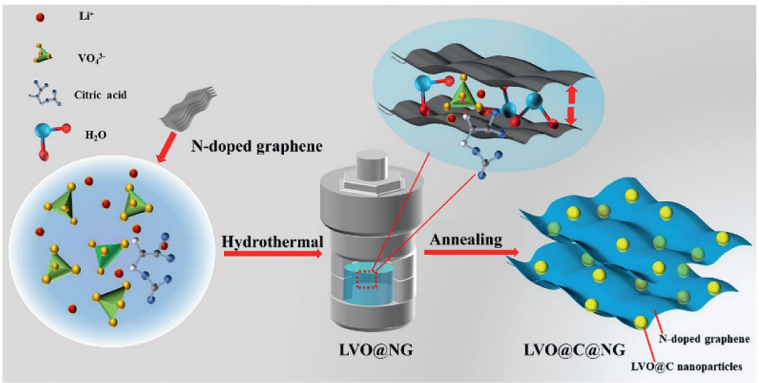

Fig. 1. Schematic diagram of the synthesis of the LVO@C@NG.

ing highly conductive supports for battery-type materials would be an efficient strategy to realize high pseudocapacitive contribution for LICs.

As a new intercalation pseudocapacitive material [15–19], Li_3VO_4 has recently received widespread attentions as anode for LICs and lithium ion batteries (LIBs) since it possesses the competitive merits of higher theoretical capacity (394 mAh/g based on two Li^+ ions insertion/extraction, and 592 mAh/g based on three Li^+ ions insertion) and lower working potential (~0.8 V *vs.* Li^+/Li) with two-electron reaction than those of other intercalation-based anode materials including $Li_4Ti_5O_{12}$ [20], $LiTi_2(PO_4)_3$ [21], TiO_2 [11], Nb_2O_5 [22], V_2O_5 [23], $TiNb_2O_7$ [24]. Owing to large structural strain and poor cycling stability caused by three Li^+ ions insertion into Li_3VO_4, such anode with two-electron reaction was usually investigated. However, the actual utilization of Li_3VO_4 is restricted by the shortcomings of large particle size and poor electronic conductivity. To solve these issues, several major strategies have been developed including nanostructure engineering, metal doping, and constructing Li_3VO_4/carbon (LVO/C) hybrids [25]. Among them, simply nanostructuring inevitably suffers from self-aggregation during repeated electrochemical cycling, resulting in reduced electrolyte access of active component. In recent years, developing Li_3VO_4/C composites has become an efficient way to realizing improving electronic conductivity, such as Li_3VO_4/amorphous carbon [26], Li_3VO_4/carbon nanotubes [27], Li_3VO_4/graphene [28]. These composites, however, undergo either limited improvement owing to amorphous carbon modification or a simply physical contact by a solid state method or wet chemical synthesis, which cannot well guarantee good electronic coupling between active nanobuilding blocks and carbon supports. Especially at a high current rate, the large structure strain caused by LVO composite would lead to large contact resistance and electrode pulverization. In addition, LVO usually exhibits a dominated pseudocapacitive contribution at a high current rate while the high capacitive contribution for LVO anode at a low current rate has been rarely reported so far. In this context, developing pseudocapacitive-dominated LVO/C hybrids with highly conductive support, robust interconnection and efficient anchoring for each active component would be highly desirable for practical application.

Herein, we report a 2D nanospace confined strategy to construct uniform LVO nanocrystals encapsulated inside the interlayers in the N-doped graphene (LVO@C@NG), which delivers much improved lithium storage performance with dominated pseudocapacitive behaviors at both low and high current rates as anode for LICs. As shown in Fig. 1, such hybrid possesses the following advantages. First, uniform LVO nanocrystals were well synthesized inside the N-doped graphene interlayers by the 2D nanospace confined strategy, which not only realizes high-quality anchoring for each active nanobuilding block but also ensures strong electronic coupling of active components and N-doped graphene (NG). Moreover, the proposed 2D space confined approach can control the size of active components. Second, the so-formed LVO@NG hybrids possess flexible graphene interlayers for well accommodating structure strain caused by repeated Li^+ intercalation and deintercalation processes at a high current rate. More importantly, the as-prepared hybrids show pseudocapacitive-dominated behaviors even at a low current rate as anode for LICs, which is very favorable for high-power and high-energy applications. Third, in this work, we provide a highly conductive NG support for constructing LVO@NG hybrids by using highly stable C_3N_4 nanosheets as template and nitrogen source without the necessity to using conventionally chemical oxidization method, which is beneficial for scalable application. The introduction of nitrogen (~3.5 wt% based on EDX mapping) in NG can modulate carbon matrix and further enhance electronic conductivity. Interestingly, in the preparation of LVO@C@NG, the graphitic degree of N-doped graphene can be improved owing to the synergistical catalytic function between vanadium oxides and NG [29], thereby leading to better electronic conductivity. Owing to these unique merits, the LVO@C@NG exhibits reversible capacities of 206 mAh/g at a high current density of 10 A/g, capacity retention of 92.7% after 1000 cycles at 2 A/g, capacitive contributions of 90.8% and 95.7% at the sweep rates of 0.2 and 1.0 mV/s, respectively, and a high energy density of 113.6 Wh/kg at 231.8 W/kg for LICs with activated carbon (AC) as cathode and LVO@C@NG as anode.

As illustrated in Fig. 1, LVO@C@NG hybrids have been prepared by a 2D nanospace confined strategy in the hydrothermal condition and subsequent solid state method. Firstly, N-doped graphene (NG) was prepared by a facile solid state reaction using C_3N_4 nanosheets as template and glucose as carbon source [30,31], and was employed as nanoreactors for the confined growth of LVO. By a hydrothermal treatment, the 2D interlayers of NG were expanded for well accommodating the precursors of LVO at the molecular scale. During the hydrothermal process, the dissolved LVO precursors and water molecules were co-intercalated into the interlayers of NG, which can effectively prevent the agglomeration of NG. In the meanwhile, the generated LVO nanocrystals will uniformly distribute in the interlayers of NG. At the subsequent annealing treatment, the highly crystalline LVO was obtained accompanying by the pyrolysis and carbonization of citric acid, generating well-confined LVO@C@NG hybrids.

The morphology and microstructure of the obtained LVO@C@NG hybrids were characterized by scanning electron microscopy (SEM), transmission electron microscopy (TEM) and high-resolution TEM (HRTEM). Firstly, ultrathin graphene layers were observed with 3–5 layers for NG (Fig. S1c in Supporting information). By using the as-prepared NG as the nanoreactors, the LVO@C@NG was synthesized by hydrothermal reaction based on the nanospace con-

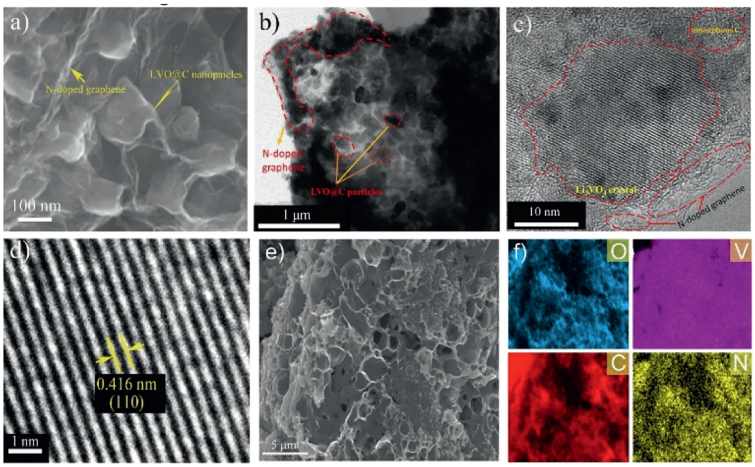

Fig. 2. (a) SEM image, (b) TEM image, (c, d) HRTEM images and (e, f) SEM image and EDX mapping images for elemental C, N, O, and V for LVO@C@NG.

fined strategy and subsequent high-temperature annealing process. As shown in Fig. 2a, LVO@C nanoparticles were well encapsulated by graphene networks, which is further confirmed by TEM (Fig. 2c). The homogeneous particle sizes with 80–100 nm for LVO were identified by TEM image (Fig. 2b), indicating that the proposed nanospace confined synthesis by the hydrothermal reaction is beneficial for the uniform growth of LVO nanocrystals. For comparison, two control samples without using NG nanoreactors (LVO@C) and with using active carbon (AC) as nanoreactors (LVO@C/AC) were prepared, respectively. As displayed in Fig. S2a (Supporting information), the obtained LVO@C/AC shows a bulk structure with 20–100 μm. High-magnification SEM image reveals that such hybrid exhibits a dense internal structure of AC, suggesting that LVO grows on the outside surface of AC with uncontrollable ways. For the LVO@C composite, it also delivers a bulk architecture with 20–40 μm. Such finding shows that the absence of NG nanoreactor is not favorable for controllable and confined growth of LVO nanocrystals, leading to large particle. This is not beneficial for developing high pseudocapacitance performance for LICs. Despite these, our prepared LVO@C@NG exhibits highly crystalline LVO with lattice spacing of 0.416 nm (Fig. 2d), corresponding to (110) crystalline plane of LVO. Elemental EDX mapping measurement (Fig. 2e) shows that the uniform elemental distributions of C, N, O, and V were confirmed in Fig. 2f.

The obtained LVO@C@NG was investigated by X-ray diffraction (XRD), Raman spectra, and X-ray photoelectron spectra (XPS). As displayed in Fig. 3a, all diffraction peaks of three samples can be well assigned to orthorhombic-phase Li_3VO_4 (JCPDS card No. 38-1247) with high crystallinity, revealing the pure phases of the as-prepared LVO@C@NG and two control samples. Raman spectrum (Fig. 3b) was used to compared LVO@C@NG and NG. The two samples both show two strong peaks at ~1344 cm^{-1} (D band) and ~1600 cm^{-1} (G band). Interestingly, the LVO@C@NG exhibits much increased the intensity of G band, revealing that the introduction of LVO into the interlayers of NG is beneficial to improving the graphitic degree of NG. This would further boost electronic conductivity. Besides the feature peaks of carbon, a strong peak at 474 cm^{-1} was also observed, which is assigned to the characteristic peak of Li_3VO_4 [32]. The carbon content in the LVO@C@NG hybrid is about 16.3% based the thermogravimetric analysis (TGA) in Fig. S3 (Supporting information). The full spectrum of XPS shows the presence of V, O, C and N peaks (Fig. 3c). The C 1s spectrum shows three peaks at 284.7, 285.6 and 289.4 eV, which are related to C=C bonding, C–N/C≡N bonding, and O–C=O bonding (Fig. 3d), respectively. The high-resolution spectrum of V 2p is shown in Fig. 3e, where the peaks at 525.2 and 517.4 eV are ascribed to V $2p_{1/2}$ and V $2p_{3/2}$ of V^{5+} spin-orbit levels while two peaks at 523.8 and 516.9 eV are belong to V^{4+} [30]. The little existence of V^{4+} species might be result from the vanadium partial reduction by carbothermal reaction at high temperature annealing. As displayed in Fig. 3f, the N 1s peak at 398.3 eV belonging to pyridinic N was identified while the peak at 400.7 eV is assigned to pyrrolic N [31]. The incorporation of nitrogen in the carbon matrix can enhance electronic conductivity and also modulate the properties of carbon scaffolds with increased surface activity and wettability in the electrolyte.

The as-prepared LVO@C@NG hybrids afford robust electronic interconnection between active components and carbon frameworks, thus enabling not only for rapid electron conduction at the interface but also for electron/ion transfer within the solid LVO nanocrystals. This would be very favorable for practical application of LICs. The electrochemical performance of LVO@C@NG was firstly evaluated by galvanostatic charge and discharge tests. For comparison, LVO@C/AC and LVO@C were investigated as well. As show in Fig. 4a and Fig. S2 (Supporting information), the discharge/charge capacities of LVO@C@NG in the second cycle are 438.1/410.2 mAh/g, much higher than those of LVO@C/AC (378.5/355.9 mAh/g) and LVO@C (358.3/342.8 mAh/g). It is note that there is obviously irreversible capacity loss in the first cycle, which is attributed to the formation of solid electrolyte interphase (SEI) layer [33]. Similar phenomenon was also observed in the cyclic voltammograms (CV) profiles (Fig. 4b). As shown in Fig. 4b, two strong cathodic peaks located at 0.71 V and 0.54 V were observed in the first cathodic scan, implying the strong interaction between LVO@C@NG and electrolyte. At the subsequent cycles, the CV profiles of LVO@C@NG exhibit good reversibility, suggesting the formation of stable SEI at the interface between active materials and electrolyte. Despite these, the obtained LVO@C@NG delivers the smallest electrochemical polarization with a voltage gap of 0.39 V (Fig. 4c), much lower than those of LVO@C/AC (0.62 V) and LVO@C (0.66 V). Such findings reveal the better Li^+ intercalation kinetics of the as-prepared LVO@C@NG.

Another attractive property of LVO@C@NG is superior rate capability. As shown in Figs. 4d and e, three samples were examined by galvanostatic charge and discharge measurement at current densities from 0.5 A/g to 10 A/g. LVO@C@NG delivers capacities of 380, 362, 331, and 241 mAh/g at the current density of 1, 2, 4, and 8 A/g, respectively. Even at a high current density of 10 A/g, it still maintains the reversible capacity of 208 mAh/g, much higher than those of LVO@C/AC (160 mAh/g) and LVO@C (89 mAh/g). When the current density is reduced to 0.5 A/g, the reversible capacity of LVO@C@NG can be well recovered, indicating excellent Li^+ storage reversibility. The superior rate capability is probably attributed

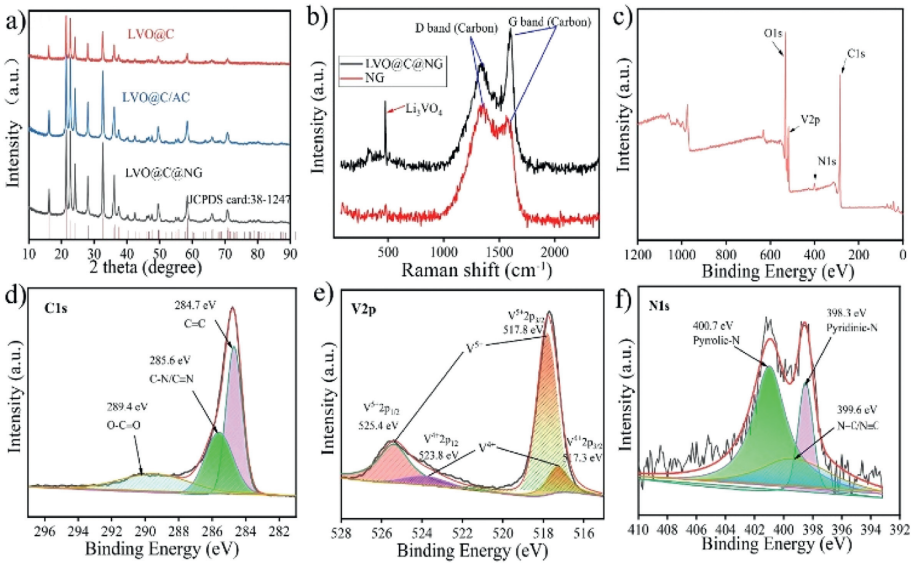

Fig. 3. (a) XRD patterns for LVO@C@NG, LVO@C, and LVO@C/AC. (b) Raman spectra, (c) full XPS spectrum for LVO@C@NG. High-resolution spectra of (d) C 1s, (e) V 2p, and (f) N 1s.

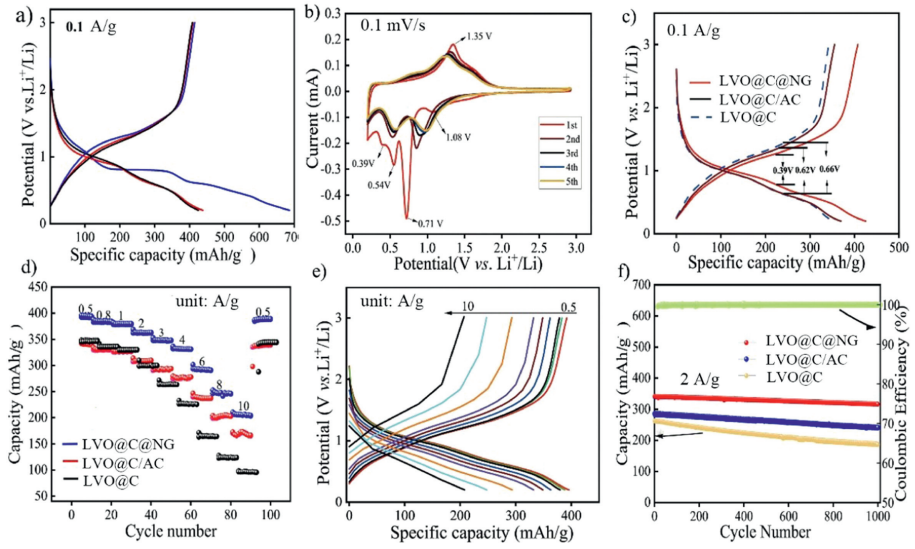

Fig. 4. Electrochemical performance for the LVO@C@NG and the control samples between 0.2–3.0 V (*vs.* Li/Li^+): (a) Galvanostatic charge-discharge profiles for LVO@C@NG. (b) CV curves of LVO@C@NG. (c) The electrochemical polarization comparison of LVO@C@NG, and LVO@C/AC, and LVO@C. (d) Rate performances of LVO@C@NG, and LVO@C/AC, and LVO@C. (e) The representative charge and discharge voltage profiles of LVO@C@NG at various current rate of 0.5, 0.8, 1.0, 2.0, 3.0, 4.0, 6.0, 8.0, and 10 A/g. (f) Cycling performance of LVO@C@NG, and LVO@C/AC, and LVO@C at 2 A/g.

to the unique LVO@C@NG structure with higher pseudocapacitive contribution, which will be further discussed in detail in the following part.

In addition to high-rate capability, long-term cycling performance is a very important factor for practical application of LICs. As shown in Fig. 4f, the three samples were evaluated for a long cycle at 2 A/g. It was found that LVO@C@NG exhibits a reversible capacity of 316 mAh/g and capacity retention of 92.7% after 1000 cycles, significantly higher than those of LVO@C/AC and LVO@C. Even at a higher current density of 4 A/g, LVO@C@NG still delivers a specific capacity of 252.7 mAh/g after 1000 cycles (Fig. S5 in Supporting information). Such findings suggest that the as-prepared LVO@C@NG hybirds with good and uniform capsulation of LVO nanocrystals in the interlays of NG and robust electronic coupling should account for the excellent lithium storage properties.

To investigate the charge storage mechanism of LVO@C@NG, CV measurements with different scanning rates were carried out, as shown in Fig. 5a. With increasing scanning rates, the current densities of oxidation/reduction peaks for LVO@C@NG were gradually enhanced. Interestingly, the peak positions for oxidation and reduction peaks do not show an evident shift, indicating the LVO@C@NG with ignorable electrochemical polarization. Generally, charge-storage process includes diffusion-controlled (battery-like) and surface-controlled (capacitor-like) responses. In the CV experiment, the current response (i) and the sweep rate (ν) obey the following relationship [34]:

$$i = a\nu^b \tag{1}$$

where a is a constant and b is the power-law exponent. According to the b value by fitting the slope of the plot of $\log(i)$ *versus* $\log(\nu)$ at a fixed potential, the information about the charge-storage mechanism can be confirmed qualitatively. When $b = 0.5$, charge storage is controlled by semi-infinite diffusion process as occurs in bulk battery materials. In contrast, for the capacitive charge-

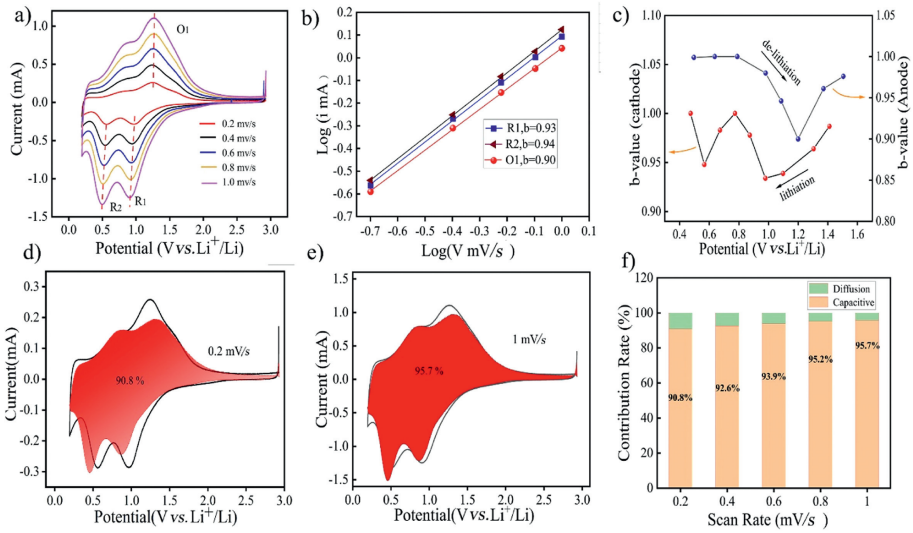

Fig. 5. Electrochemical behavior analysis of lithium storage process of LVO@C@NG electrode. (a) CV curves at different scanning rates. (b) log(*i*) *versus* log(*v*) plots at specific current peaks. (c) *b* values change with the potential, CV curves of capacitive contribution at (d) 0.2 mV/s, and (e) 1.0 mV/s. (f) Normalized capacitive and diffusion contribution at different sweep rates.

storage mechanism (surface-controlled), *b* is equal to 1. We analyzed the redox-peaks *b* values of the LVO@C@NG, where the results are presented in Fig. 5b. The calculated *b* values for cathodic and anodic peaks are 0.93 (R1), 0.94 (R2) and 0.90 (O1), suggesting that a capacitive-dominated charge-storage process. Moreover, the broadened redox peaks can be observed that is totally different from the quasi-rectangle capacitor profiles, which implies the existence of electrochemical behaviors associated with pseudocapacitance response. Furthermore, we also investigated the variable *b* values of the entire operating potential range. As shown in Fig. 5c, during the lithiation process, when $b=1$ at the potential of 1.5 V that is far from the redox regime represents an electrical double-layer charging process. With the lithiation potential decreases, Li^+ storage in the LVO@C@NG occurs accompanying by the reduction of *b* value. When the potential is reduced below 0.9 V, the *b* value underwent a sudden increase and was gradually close to 1. These results indicate that Li^+ ions are probably depleted at the electrode/electrolyte interface and then generates a new electrical double layer lithiation process.

Using the concepts presented above, the current at a fixed potential is the sum of two types of charge-storage contributions that results from capacitive contribution and diffusion-controlled insertion processes. Hence, the CV current (*i*) can be divided into two parts by the following Eq. 2 [35]:

$$i_{(V)} = k_1 \nu + k_2 \nu^{1/2} \quad (2)$$

where $k_1\nu$ corresponds to the current contribution from the surface capacitive effects while $k_2\nu^{1/2}$ is the diffusion-controlled intercalation process contributed current. Base on this equation, the contribution ratio between the two different charge storage processes at different scanning rates is confirmed. At a relatively slow sweep rate of 0.2 mV/s (Fig. 5d), the capacitive contribution accounts for 90.8% and 95.7% in the total charge storage, where the capacitive charge storge is mainly from pseudocapacitance. Compared to the reported LVO anode [18,19,36], the obtained LVO@C@NG show the highest capacitance contribution at the low current scanning rate. When the sweet rates are gradually increased, the capacitance contribution was also enhanced. At 1 mV/s, the pseudocapacitive behavior is highly dominant with a contribution of 95.7% (Figs. 5e and f). It was found that the as-prepared LVO@C@NG exhibits a dominant pseudocapacitance behavior, which is very beneficial for high-performance LICs. Owing to the unique architectures, homogeneously distributed LVO nanocrystals were well anchored in the 3D graphene frameworks, which can not only guarantee high-efficiency utilization of active materials, but also provide abundant accessible sites, thus enabling pseudocapacitance dominated lithium storage behaviors. In the meanwhile, the N-doped graphene networks could also facilitate rapid charge transportation and ensure the structural stability. Owing to the above two aspects, the obtained LVO@C@NG shows much enhanced pseudocapacitance dominated lithium storage behaviors.

To probe the charge transport kinetics of the LVO@C@NG, electrochemical impedance spectroscopy (EIS) was performed, as shown in Fig. S6 (Supporting information). According to the fitting results, the ohmic resistance of LVO@C@NG electrode material is 4.5 Ω, lower than those of LVO@C/AC anode (5.7 Ω) and LVO@C anode (6.3 Ω). The results suggest that constructing LVO@C@NG hybrids assembled from well-capsulated LVO nanoparticles in N-doped graphene with strong interconnection and electronic coupling is an efficient strategy to lower contact resistance. Moreover, LVO@C@NG electrode exhibits the smallest charge transfer resistance R_{ct} (72.65 Ω) than those of LVO@C/AC (97.72 Ω) and LVO@C (83.05 Ω), revealing faster reaction kinetics. During the subsequent cycles, the R_{ct} value of LVO@C@NG gradually decreases from 10.64 Ω (the third cycle) to 0.49 Ω (the 10^{th} cycle) with the continuous activation process, suggesting that the charge transport barrier was remarkably reduced after activation processes.

Benefiting from the excellent electrochemical performance of LVO@C@NG for lithium storage, LVO@C@NG was employed as anode for evaluating its electrochemical behaviors of LICs with commercial AC as cathode (Figs. 6a and b). For comparison, commercial AC cathode and Li metal anode were assembled and evaluated (Fig. S7 in Supporting information). The AC half-cell delivers linear voltage profile in the potential range between 2.0 V and 4.4 V (Fig. S7a) with a reversible specific capacity of 56 mAh/g at 0.5 A/g. As displayed in the CV tests (Fig. S7b), rectangular profiles can be observed, implying that the reaction is a non-faradaic capacitive process. The excellent rate capability of AC can be obtained owing to the rapid non-faradaic capacitive behavior (Fig. S7c), and it also exhibits a stable cycle life after 1000 cycles (Fig. S7d). The CV curves of AC//LVO@C@NG display quasi-rectangular shapes, which is different from the rectangular shape of the traditional EDLCs (Fig. 6c), suggesting the combination of two different charge storage mech-

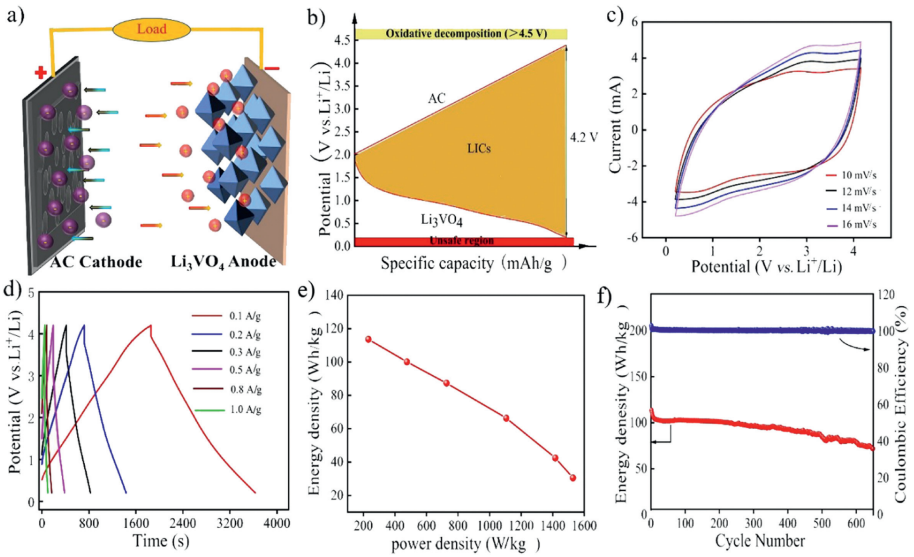

Fig. 6. Electrochemical performance of AC//LVO@C@NG LICs: (a) Schematic illustration for LICs. (b) Voltage profiles and electrochemical reaction mechanism of LICs. (c) CV curves at various scanning rates from 10 mV/s to 16 mV/s. (d) Charge/discharge profiles at various current densities from 0.1 A/g to 1 A/g. (e) Ragone plots and (f) cycle performance at the current density of 0.1 A/g.

anisms. In general, the commercial AC cathode storages charge mainly through the adsorption reaction of PF_6^- anions while LVO anode is based on the faradaic reaction of Li^+ intercalation into LVO@C@NG. The totally different charge storage mechanism between the two electrodes causes a "transition" shape of the CV curves. The charge and discharge curves shapes of AC//LVO@C@NG exhibit symmetric *quasi*-triangles (Fig. 6d), which is consistent with the CV results. Despite these, the AC//LVO@C@NG LICs deliver a high energy density of 113.6 Wh/kg at the power density of 231.8 W/kg. Even at a high power density of 1529 W/kg, the energy density of 30.6 Wh/kg can still be maintained (Fig. 6e), indicating good kinetics balance between AC cathode and LVO@C@NG anode. In addition, such AC//LVO@C@NG LICs can remain an energy density of 70.1 Wh/kg after 650 cycles (Fig. 6f).

In summary, we have developed a facile and efficient 2D nanospace confined strategy to prepare well encapsulated LVO in the interlayers of highly conductive graphene supports and demonstrated their applications for LIBs and LICs. The obtained LVO@C@NG hybrids afford intimate electronic coupling between active materials and N-doped graphene, thus resulting in both more active sites and robust structural stability than each nanobuilding block alone or their simple physical contact. Benefiting from these unique merits, such hybrids show pseudocapacitance dominate lithium storage behaviors with capacitive contribution of 90.8% even at a low sweep rate of 0.2 mV/s. When employed as anode for LICs, such hybrids show superior rate capability and excellent cycling stability with reversible capacities of 206 mAh/g at a high current density of 10A/g, capacity retention of 92.7% after 1000 cycles at 2 A/g, and a high energy density of 113.6 Wh/kg at 231.8 W/kg for LICs.

Declaration of competing interest

The authors declare that they have no known competing financial interests or personal relationships that could have appeared to influence the work reported in this paper.

Acknowledgments

This work was financially supported by the National Natural Science Foundation of China (Nos. 52001059, 52072119), Hunan Provincial Natural Science Foundation (No. 2023JJ50015), the 111 Project (No. D20015).

Supplementary materials

Supplementary material associated with this article can be found, in the online version, at doi:10.1016/j.cclet.2024.109675.

References

[1] A. Jagadale, X. Zhou, R. Xiong, et al., Energy Storage Mater. 19 (2019) 314–329.
[2] L. Jin, C. Shen, A. Shellikeri, et al., Energy Environ Sci. 13 (2020) 2341–2362.
[3] W. Liu, Y. An, L. Wang, et al., J. Energy Chem. 80 (2023) 68–76.
[4] L. Wang, X. Zhang, C. Li, et al., Chem. Eng. J. 468 (2023) 143507.
[5] N.S. Choi, Z. Chen, S.A. Freunberger, et al., Angew. Chem. Int. Ed. 51 (2012) 9994–10024.
[6] L. Wang, X. Zhang, Y. Xu, et al., Adv. Funct. Mater. 31 (2021) 2104286.
[7] L. Wang, X. Zhang, C. Li, et al., Rare Metals 41 (2022) 2971–2984.
[8] B. Li, J. Zheng, H. Zhang, et al., Adv. Mater. 30 (2018) 1705670.
[9] V. Augustyn, P. Simon, B. Dunn, Energy Environ. Sci. 7 (2014) 1597–1614.
[10] R. Marchand, L. Brohan, M. Tournoux, Mater. Res. Bull. 15 (1980) 1129–1133.
[11] M. Zukalová, M. Kalbác, L. Kavan, I. Exnar, M. Graetzel, Chem. Mater. 17 (2005) 1248–1255.
[12] M. Okubo, E. Hosono, J. Kim, et al., J. Am. Chem. Soc. 129 (2007) 7444–7452.
[13] M. Okubo, Y. Mizuno, H. Yamada, et al., ACS Nano 4 (2010) 741–752.
[14] H.S. Kim, J.B. Cook, S.H. Tolbert, B. Dunn, J. Electrochem. Soc. 162 (2015) A5083.
[15] C. Liao, Q. Zhang, T. Zhai, H. Li, H. Zhou, Energy Storage Mater. 7 (2017) 17–31.
[16] C. Zhang, H. Song, C. Liu, et al., Adv. Funct. Mater. 25 (2015) 3497–3504.
[17] H.Tran Huu, N.H. Vu, H. Ha, et al., Nat. Commun. 12 (2021) 3081.
[18] W. Liu, X. Zhang, C. Li, et al., Chin. Chem. Lett. 31 (2020) 2225–2229.
[19] X. Ren, D. Ai, C. Zhan, et al., Electrochim. Acta 355 (2020) 136819.
[20] G. Wang, C. Lu, X. Zhang, et al., Nano Energy 36 (2017) 46–57.
[21] J.Y. Luo, Y.Y. Xia, J. Power Sources 186 (2009) 224–227.
[22] Z. Chen, H. Li, X. Lu, et al., ChemElectroChem 5 (2018) 1516–1524.
[23] Y. Yue, H. Liang, Adv. Energy Mater. 7 (2017) 1602545.
[24] W. Zhu, B. Zou, C. Zhang, et al., Adv. Mater. Interfaces 7 (2020) 2000705.
[25] Q. Li, Q. Wei, J. Sheng, et al., Adv. Sci. 2 (2015) 1500284.
[26] Z. Liang, Y. Zhao, Y. Dong, et al., Electroanal. Chem. 745 (2015) 1–7.
[27] H. Cheng, Y. Zhang, X. Cai, et al., Small (2023) 2305762.
[28] M. Zhang, R. Bai, S. King, et al., Energy Storage Mater. 43 (2021) 482–491.
[29] Q. Hu, J.Y. Liao, X.D. He, et al., J. Mater. Chem. A 7 (2019) 4660–4667.
[30] C. Yang, Y. Ran, C. Gao, Z. Wang, Y.L. Ding, J. Alloy Compd. 918 (2022) 165668.
[31] Y.L. Ding, P. Kopold, K. Hahn, et al., Adv. Funct. Mater. 26 (2016) 1112–1119.
[32] H. Park, W. Jae, J. Kim, J. Alloy Compd. 767 (2018) 657–665.
[33] C. Liao, Y. Wen, B. Shan, T. Zhai, H. Li, J. Power Sources 348 (2017) 48–56.
[34] Z. Jian, M. Zheng, Y. Liang, et al., Chem. Commun. 51 (2015) 229–231.
[35] T. Brezesinski, J. Wang, S.H. Tolbert, B. Dunn, Nat. Mater. 9 (2010) 146–151.
[36] L. Zhu, Z. Li, G. Ding, et al., J. Mater. Sci. Technol. 89 (2021) 68–87.